QUARTERLY JOURNAL OF THE ROYAL METEOROLOGICAL SOCIETY
Q. J. R. Meteorol. Soc. **00**: 1–12 (2008)
Published online in Wiley InterScience
(www.interscience.wiley.com) DOI: 10.1002/qj.000

Spontaneous-adjustment emission of inertia-gravity waves by unsteady vortical motion in the hurricane core

E. A. Hendricks[a*], W. H. Schubert[b], S. R. Fulton[c], and B. D. McNoldy[b]
[a]*Naval Research Laboratory, Monterey, CA USA*
[b]*Colorado State University, Fort Collins, CO USA*
[c]*Clarkson University, Potsdam, NY USA*

Abstract: It is well known that intense atmospheric vortices have the potential to spontaneously radiate inertia-gravity waves (IGWs) to the environment via frequency matching between the unsteady vortical motion and an intrinsic IGW, provided the Rossby number is greater than unity. In the present work we undertake an analysis of a shallow water simulation of an actively radiating hurricane-like vortex to understand the nature of the emitted spiral waves, and to obtain theoretical insight into the ultimate implications of such radiation on the vortex tangential momentum and kinetic energy. The initial condition is motivated by observations of hurricanes with elliptically-shaped eyewalls, and it consists of an offset vorticity monopole in an elliptically shaped vorticity ring. The simulated lifecycle proceeds in two phases. The first phase (lasting approximately 12 h) is marked primarily by inner-core vorticity mixing and rearrangement. The second phase (lasting 36 h) is marked by a prolonged episode of spontaneous adjustment emission of spiral IGWs to the environment. During the radiation phase, we find that unsteady vortical motion in the core is a IGW source, constraining both the frequency and radial wavenumber of the emitted waves. Additionally, a Rossby-IGW instability causes both the source vortex Rossby wave and IGWs to amplify in tandem. We also find that the IGWs are sufficiently small amplitude that quasi-balance is preserved. The consequences of this are two-fold. First, the sustained outward radiation of IGWs to the environment does not significantly decrease the intensity of the mean vortex (only a 1.5% decrease in kinetic energy in 36 h, part of which is caused by nonconservative damping). Rather, vorticity mixing in the early phase is found to be much more significant. Secondly, the fuzziness of the slow manifold here is found to be exponentially small because a balance (nondivergent) model using vorticity advection and inversion is sufficient for obtaining the important features of the flow. Based on these results, we hypothesize that intense hurricanes may often enter into spontaneously radiative states, that these states are not likely to be observed, and that the emission of IGWs from their cores is not important for their amplification or decay. The validity of these idealized quasi-linear barotropic results needs to be tested using more complex baroclinic vortices and with the inclusion of moist processes and nonlinear feedbacks.

KEY WORDS inertia-gravity waves; hurricane; spontaneous adjustment; imbalance

Received 15 December 2008

1 Introduction

Although in an axisymmetric sense, the tropical cyclone (TC) is a balanced vortex (Willoughby 1990), balance is often disrupted in localized regions by latent heat release from deep convection. During the ensuing gradient adjustment process a significant amount of that energy can be radiated into the environment in the form of inertia-gravity waves (Schubert et al. 1980). Yet, an even more subtle mechanism of producing these inertia-gravity waves (hereafter IGWs) is an unforced balance adjustment, or *spontaneous radiation* from unsteady vortical motion in the TC core. This mechanism can be generally be regarded as the opposite of a balance adjustment (Ford et al. 2000). The slow manifold (Leith 1980) is an atmospheric invariant completely devoid of such gravity wave activity. The flow is balanced, and it, along with the geopotential, may be obtained at any instant by potential vorticity (PV) inversion. The existence (Lorenz 1986) or nonexistence (Lorenz and Krishnamurthy 1987) of such a strict slow manifold in the real atmosphere has been debated for decades.

In a pioneering paper, Lighthill (1952) explicitly defined the concept of spontaneous adjustment emission of sound waves from vortical flow through multiscale frequency matching. These ideas were extended to spontaneous IGW radiation from vortical flows in the atmosphere using the shallow water equations (Ford 1994a,b), in which the Froude number replaces the Mach number. The question that arises is whether or not spontaneous IGW emission is of meteorological significance from an energy and angular momentum budget perspective, which ultimately lies at the heart of the validity of the balance approximation and potential vorticity inversion. While it is generally regarded that the strict slow manifold rarely, if ever, exists, the level of fuzziness is not well understood. Saujani and Shepherd (2002) and Vanneste and Yavneh (2004) have argued that the fuzziness is exponentially small for quasigeostropic flow. Moreover, the characteristics of a given balanced flow that favor its potential to

*Correspondence to: Dr. Eric A. Hendricks, Naval Research Laboratory, 7 Grace Hopper Ave, Stop 2, Monterey, CA 93940. Email: eric.hendricks@nrlmry.navy.mil

spontaneously radiate are not well understood (Viudez and Dritschel 2006).

Spontaneous IGW radiation has recently been examined in theoretical studies and numerical model simulations of both atmospheric jets (e.g., Uccellini and Koch 1987, O'Sullivan and Dunkerton 1995, Zhang 2004) and vortices (e.g., Ford et al. 2000, Plougonven and Zeitlin 2002, Schecter and Montgomery 2006, Viudez 2006, Snyder et al. 2008). In addition, the phenomenon has been examined in laboratory experiments (e.g., Lovegrove et al. 2000, Afanasyev 2003, Williams et al. 2005). Schecter and Montgomery (2006) examined conditions that favor spontaneous radiation from intense mesocyclones such as tornadoes and hurricanes. One interesting result from their study was that under certain conditions vortex Rossby waves on monotonic cyclones can grow due to a positive feedback from the spontaneous IGW emission. IGWs have also been hypothesized to create the moving spiral cloud bands in tropical cyclones that are often visible in satellite imagery (Kurihara 1976, Willoughby 1977, Chow et al. 2002). This is in contrast to theories ascribing their existence to breaking vortex Rossby waves (Guinn and Schubert 1993, Montgomery and Kallenbach 1997). Chow and Chan (2004) argued that IGWs may be an important sink of angular momentum from the hurricane.

To a first approximation, a tropical cyclone is an axisymmetric vortex because differential rotation of the swirling winds causes the decay of asymmetries (or axisymmetrization), by which eddy momentum is transferred to the mean vortex. However, it is well known that the hurricane core is often observed to be asymmetric, commonly with low wavenumber deformations (e.g., Kuo et al. 1999, Reasor et al. 2000). The generation of these asymmetries may be linked to deep convection (Montgomery and Enagonio 1998) or from dynamic instability of the swirling winds (Schubert et al. 1999). Due to the large vorticity in tropical cyclone core, it is expected that unsteady asymmetric vortical motion may oscillate at a frequency greater than the background rotation and therefore have the potential to spontaneousy radiate IGWs (Ford et al. 1994, Schecter and Montgomery 2004).

Here, we undertake an analysis of IGW radiation from unsteady vortical motion in the TC core, and examine the ultimate implications of such radiation for TC intensity change. To that end, we have simulated an unforced dynamically active, spontaneously radiating, hurricane-like vortex using a shallow water model. The initial condition consists of an monopole in an elliptically shaped ring, and is motivated by observations of elliptically shaped eyewalls that are often observed in hurricanes. Although the initial condition is balanced, the system quickly evolves into a state of quasi-balance, with small amplitude, large spiral IGWs being emitted radially outward. Based on this simulation, we will demonstrate that this emission is not significant for the intensity change of the mean vortex. Rather, we will show that vorticity mixing is the primary cause of the minor weakening that occurred. In section 2, the dynamical models used in this study are described. In section 3, the evolution in the shallow water model is examined. In section 4, the linearized results are shown to understand aspects of the nonlinear shallow water simulation, including multiscale frequency matching and Lighthill emission. The conclusions are given in section 5.

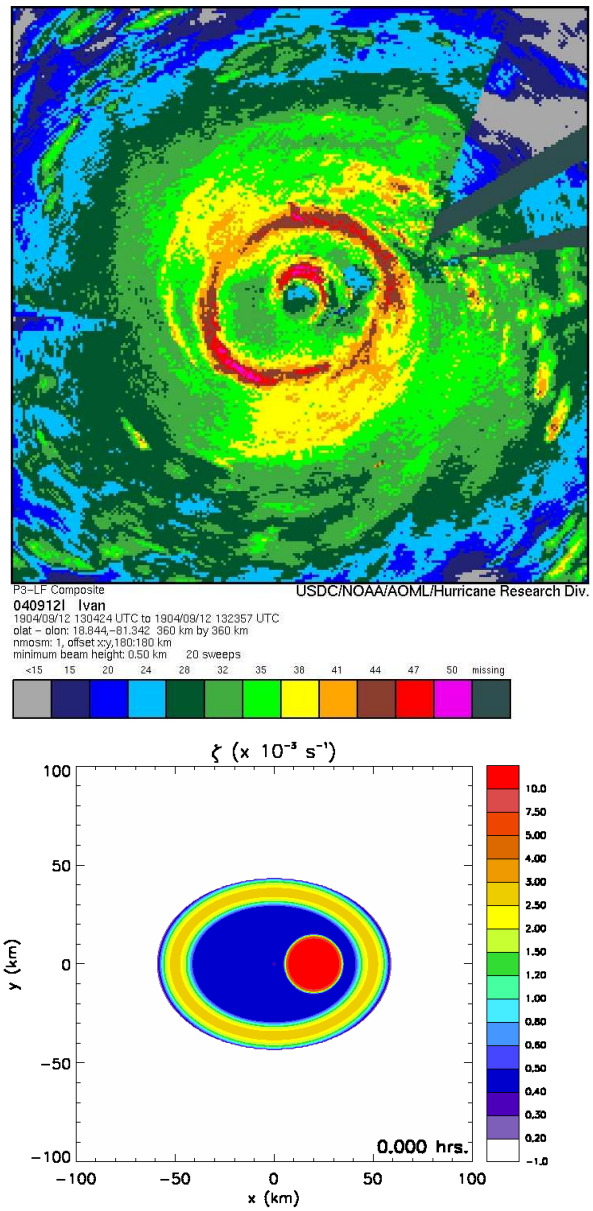

Figure 1. (top panel) Composite radar reflectivity (dBz) of Hurricane Ivan between 1304 and 1325 UTC on 12 September 2004. The domain is 360 km by 360 km. Courtesy of NOAA/AOML/Hurricane Research Division, and (bottom panel) the relative vorticity ζ at $t = 0$ h in the shallow water experiment. The divergence δ is initially zero and the height field is balanced.

2 Dynamical models

2.1 Shallow water model

We use a shallow water model because it is simplest model that contains Rossby and IGW wave solutions. For a shallow water fluid, the vector momentum equation in

DOI: 10.1002/qj

rotational form is

$$\frac{\partial \mathbf{u}}{\partial t} + (f+\zeta)\mathbf{k}\times\mathbf{u} + \nabla\left(gh + \tfrac{1}{2}\mathbf{u}\cdot\mathbf{u}\right) = 0, \quad (1)$$

where $\mathbf{u}$ is the horizontal velocity vector, f the constant Coriolis parameter, $\mathbf{k}$ the vertical unit vector, $\zeta = \mathbf{k}\cdot\nabla\times\mathbf{u}$ the relative vorticity, g the acceleration of gravity, and h the deviation of the free surface height from the constant mean value $\bar{h}$. By taking $\nabla\cdot$ and $\mathbf{k}\cdot\nabla\times$ of (1), we obtain the divergence and vorticity equations in the form

$$\frac{\partial \delta}{\partial t} + \nabla\cdot\{(f+\zeta)\mathbf{k}\times\mathbf{u}\} + \nabla^2\left(gh + \tfrac{1}{2}\mathbf{u}\cdot\mathbf{u}\right) = 0, \quad (2)$$

$$\frac{\partial \zeta}{\partial t} + \nabla\cdot\{(f+\zeta)\mathbf{u}\} = 0, \quad (3)$$

which, along with the continuity equation

$$\frac{\partial h}{\partial t} + \nabla\cdot\left\{(\bar{h}+h)\mathbf{u}\right\} = 0, \quad (4)$$

form the basis of our divergent barotropic model simulations. By introducing the velocity potential χ and the streamfunction ψ , the vector velocity can be expressed as $\mathbf{u} = \mathbf{u}_\chi + \mathbf{u}_\psi$, where the irrotational part of the flow is given by $\mathbf{u}_\chi = \nabla\chi$ and the nondivergent part of the flow by $\mathbf{u}_\psi = \mathbf{k}\times\nabla\psi$, implying that $\nabla^2\psi = \zeta$ and $\nabla^2\chi = \delta$.

The solutions presented here were obtained with a double Fourier pseudospectral code, using a 600 km $\times$ 600 km domain with 1024 $\times$ 1024 points. After dealiasing of the quadratic advection terms, 370 Fourier modes were kept, yielding an effective resolution of 1.8 km. To control spectral blocking, ordinary ∇^2 diffusion terms to included on the right hand sides of the prognostic equations (2)–(4). The diffusion coefficient was set to 25 m^2 s^{-1}, yielding an $1/e$-damping time of 0.19 h for all modes having total wavenumber 370. Time differencing was accomplished using a third order scheme with a time step of 1 s. The simulation was executed for 48 h, with output saved at 180 s intervals. A sponge layer with Rayleigh damping was used near the lateral boundaries to damp outward-propagating IGWs. The lateral extent of the sponge layer was 60 km, and the Rayleigh damping coefficient was smoothly increased from zero to a maximum value of 0.00278 s^{-1} as the edge of the domain was approached. This corresponds to an $1/e$-damping time of 0.10 h for all three prognostic variables near the boundary.

2.2 Nondivergent barotropic model

The same experiment was also executed using a nondivergent barotropic model that does not permit IGWs. The governing vorticity equation is

$$\frac{\partial \zeta}{\partial t} + \mathbf{u}_\psi\cdot\nabla\zeta = \nu\nabla^2\zeta, \quad (5)$$

where $\mathbf{u} = \mathbf{k}\times\nabla\psi$ is the horizontal, nondivergent velocity, $\zeta = \nabla^2\psi$ is the relative vorticity, and ν is the constant viscosity. The solutions to this model were also obtained using a doubly periodic pseudospectral code with the same numerical parameters as the shallow water code. This experiment will be compared to the shallow water model experiment to examine the effect of IGW radiation on the evolution.

3 Shallow water model simulation

The shallow water simulation is motivated by observations of hurricanes with elliptically shaped eyewalls. One such example of this occurred in Hurricane Ivan (2004), shown in the top panel of Fig. 1. Here the composite radar reflectivity from 1304 UTC to 1325 UTC is shown on September 12, 2004. At this time, Ivan had concentric eyewalls, with the outer eyewall taking on a distinctly elliptical shape. Noting the high correlation between radar reflectivity and low level relative vorticity, an idealized vorticity field was contructed. To simplify the initial condition, the inner eyewall was modeled as a monopole.

Figure 2 displays side-by-side plots of the relative vorticity and divergence in the central part of the domain for $t = 0.5, 2.5, 10$ hours. The vorticity field evolves as follows. By $t = 0.5$ h, the differential rotation associated with the strong central monopole has deformed the outer ring. This initial deformation of the outer ring is quite similar to that found in the contour dynamics experiments of Oda et al. (2006). By $t = 2.5$ h, the initial low vorticity moat region has been separated into two pieces: a nearly axisymmetric inner region just outside the central monopole, and an outer region to the north-northwest. By $t = 10$ h, very low vorticity environmental air has been enclosed approximately 30 km west of the central monopole. At this time, the vortex can be characterized as a tripole (i.e., a radial profile of high-low-high vorticity) in the y-direction and a pentapole in the x-direction through the origin. Examining the divergence (right panels of Fig. 2), a persistent wavenumber-2 feature is present. This is the response of the mass field to the propagating wavenumber-2 vortex Rossby wave, or elliptical deformation of the central monopole. Outward propagating IGWs are being emitted from the vortex core and the vortex can be considered to be spontaneously radiating very early.

The evolution of the vortex at later times ($t = 20, 30, 45$ h) is shown in Fig. 3. The central monopole now has a stronger elliptical signature, and the eccentricity becomes larger with time. The pentapole structure is evident, and the ellipse and outer low vorticity regions are rotating at different rates, causing them to come in and out of phase. In the divergence plots, outward propagating IGWs are evident and the amplitude has increased significantly from earlier times. This simulation was run to $t = 48$ h, with no apparent reduction in IGW activity at this time.

Figure 4 shows (x, t)-sections of the relative vorticity and divergence from $t = 24$ h to $t = 25$ h. The plots were made by taking a cross-section at fixed y through the vortex center at each time. In the top panel, the important features to note are the semi-major axis a and semi-minor axis b of the rotating elliptical vorticity core. The period of the ellipse oscillation is $\tau_e = 0.25$ h (or 900 s), corresponding to a frequency $\nu_e = 6.98 \times 10^{-3}$ s^{-1}. The period of the outer low vorticity patch is longer, $\tau_o = 0.65$ h (or 2340 s), corresponding to a frequency $\nu_o = 2.69 \times 10^{-3}$ s^{-1}. During the simulation, the outer structures and inner structures move in and out of phase, contributing to non-axisymmetrization. In the bottom panel, the

DOI: 10.1002/qj

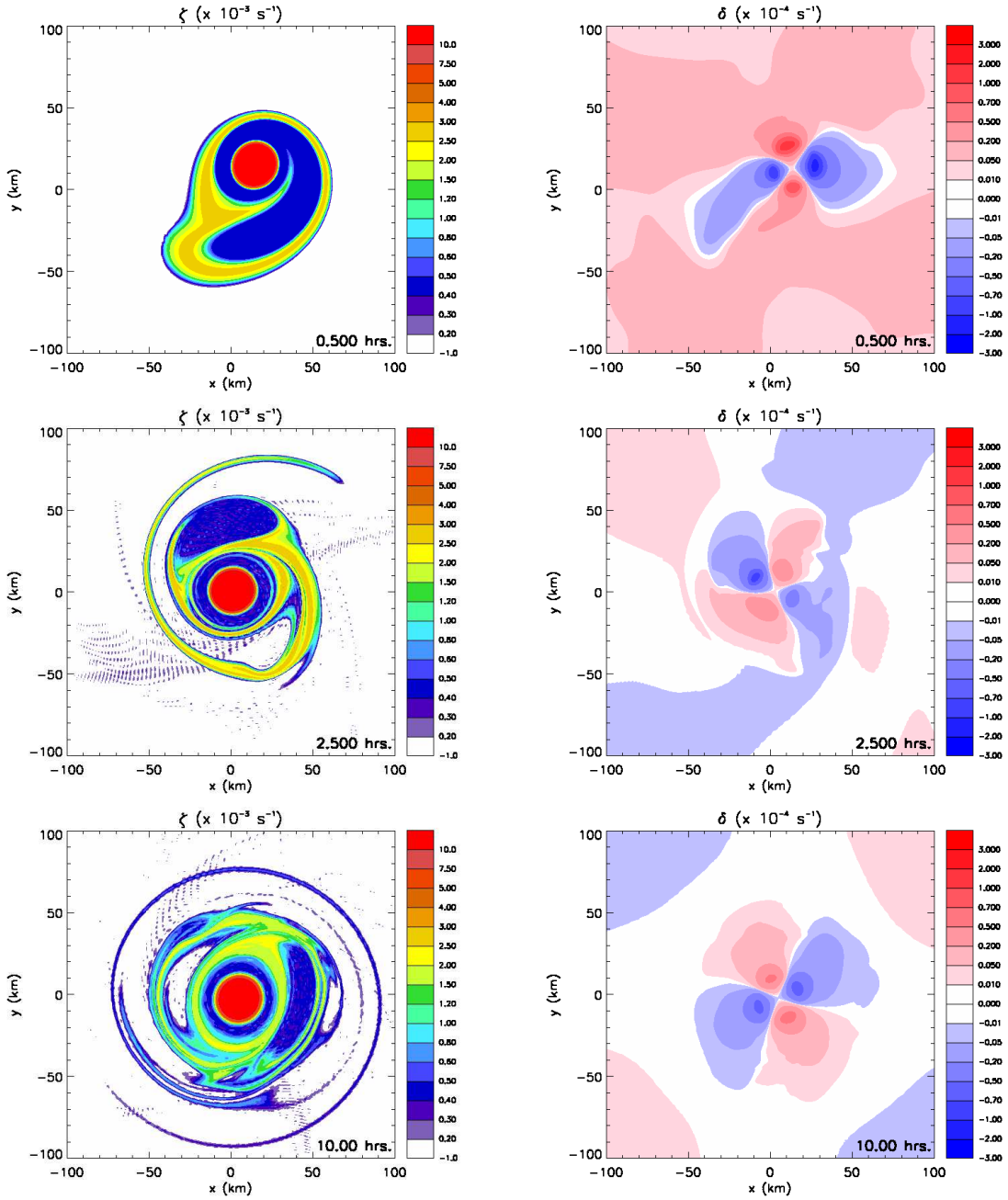

Figure 2. Early evolution ($t = 0.5, 2.5, 10$ hours) of relative vorticity (left panels) and divergence (right panels) in the shallow water experiment.

important features are the outward propagating IGWs. The phase speed of these IGWs appears to be constant, and can be estimated from the figure. For example, the area of convergence with the arrow over it propagates approximately 110 km in a time period of 0.15 h. The phase speed associated with this is c=(110000 m)/(540 s)=203.7 m s^{-1}, which is very close to the phase speed $c = 205$ m s^{-1} supported by the mean fluid depth of $\bar{h} = 4284$ m. The period of the IGWs can be ascertained from two places: near the ellipse and in the outer domain. Both locations give the same $\tau_{\rm IG} = 0.25$ h (or 900 s), corresponding to a frequency $\nu_{\rm IG} = 6.98 \times 10^{-3}$ s^{-1}. Lastly, the radial wavelength of the waves is determined from the diagram: $L_{\rm R} \approx 225$ km (or a half wavelength of 112.5 km). This corresponds to a radial wavenumber $k = 0.028$ km^{-1}. One can verify that the parameters above satisfy the dispersion relation

$$k^2 = \frac{(\nu - \bar{\omega}m)^2 - (f + 2\bar{\omega})^2}{g\bar{h}} \qquad (6)$$

using $\bar{\omega} = 0.0005$ s^{-1} away from the central region (see Fig. 7).

Note that $\nu_{\rm e} = \nu_{\rm IG} = 6.98 \times 10^{-3}$ s^{-1}, which indicates that frequency matching has occured between the rapidly oscillating ellipse and an intrinsic IGW frequency. Plotting the dispersion relation (6) in Fig. 5,

DOI: 10.1002/qj

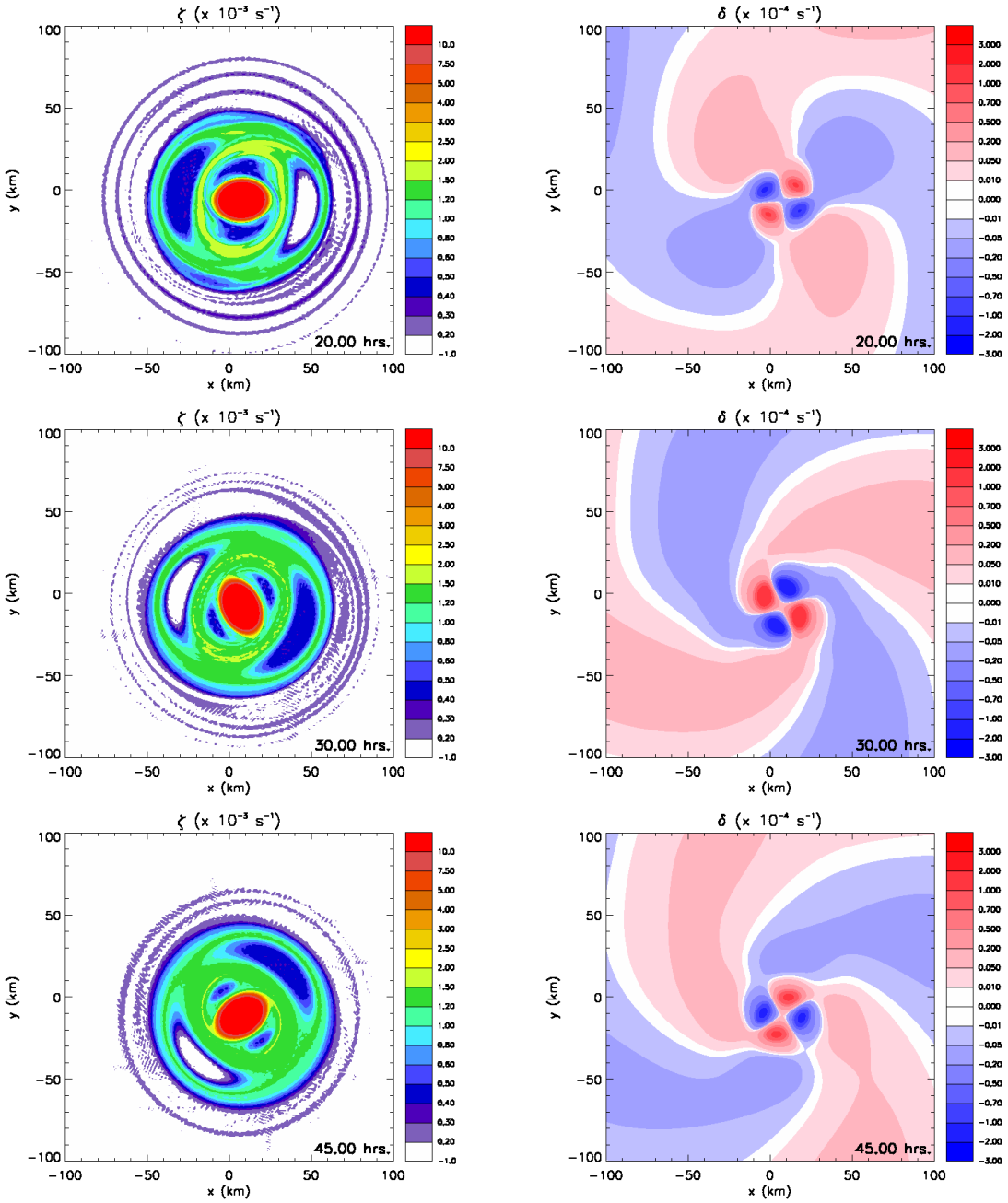

Figure 3. Later evolution ($t = 20, 30, 45$ hours) of relative vorticity (left panels) and divergence (right panels) in the shallow water experiment.

note that the frequency-matched radial wavenumber $k = 0.028$ km^{-1}. To summarize, a rapidly oscillating, non-axisymmetrizing, ellipse evolves out of the unforced initial condition of the experiment. The oscillation frequency of the ellipse matches an intrinsic IGW frequency, causing outward wave radiation to the environment of a preferred radial wavenumber ($k_{\rm R} = 0.028$ km^{-1}). Note that there is a subtle but important difference between the frequency matching here and that of Lighthill's acoustic theory. In the former, there exists a low frequency cutoff equal to the background rotation, while in the latter the dispersion curve goes through the origin (Saujani and Shepherd 2002). Thus, spontaneous emission of IGWs may only proceed if the unsteady vortical motion proceeds at a higher frequency than $f + 2\bar{\omega}$.

Why does the rapidly oscillating ellipse not axisymmetrize? Dritschel (1998) has shown that the ability of a non-axisymmetric vorticity core to axisymmetrize via inviscid nondivergent dynamics is dependent on the sharpness of its edge. Rankine-like vortices (i.e, possessing a sharp edge) are not as likely to axisymmetrize as Gaussian-like vortices because they cannot generate filaments as easily. The filamentation process is a sign of axisymmetrization. The ellipse in the experiment has a very sharp edge, with the relative vorticity ζ dropping an order of magnitude (from 1×10^{-2} s^{-1} to 1×10^{-3} s^{-1})

DOI: 10.1002/qj

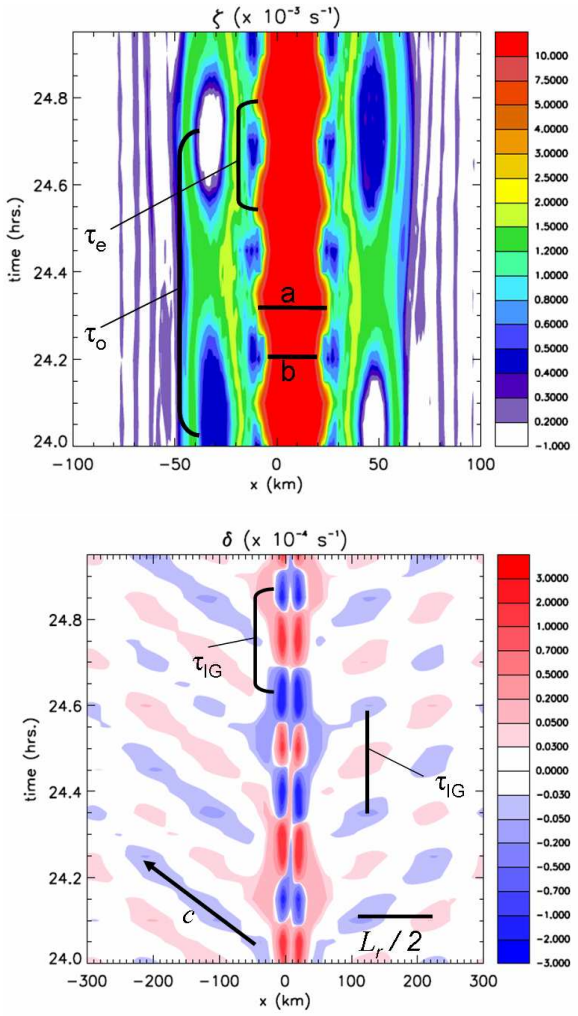

Figure 4. Hovmöller plots of relative vorticity (top panel) and divergence (bottom panel) in the shallow water simulation from $t = 24$ h to $t = 25$ h. In the top panel, a and b denote the semi-major and semi-minor axes of the central ellipse, $\tau_{\rm e}$ denotes the oscillation period of the central ellipse, and $\tau_{\rm o}$ is the oscillation period of the outer low vorticity regions. In the bottom panel, $c = (g\bar{h})^{1/2} = 205$ m s^{-1} is the pure gravity wave phase speed, $\tau_{\rm IG}$ is the inertia-gravity wave period and $L_{\rm R}$ is the radial wavelength.

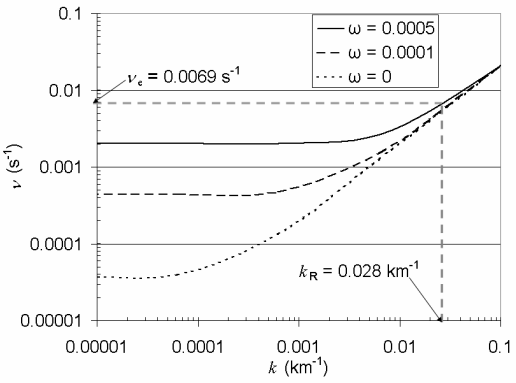

Figure 5. IGW frequency versus radial wavenumber for $c = 205$ m s^{-1} and $f = 3.7 \times 10^{-5}$ s^{-1}. Three curves are shown for varying $\bar{\omega}$ = 0, 0.0001, and 0.0005 s^{-1}. Note that the curves differ most at low wavenumbers and have different low frequency cutoffs: $f + 2\bar{\omega}$.

in approximately 3–5 km. Also note that in Fig. 4, strong vorticity filaments are not being created. At $t = 45$ h, two thin weak filaments are evident, but at other times it is hard to find filaments. Thus it is likely that the ellipse's sharp edge is contributing to non-axisymmetrization. Vorticity structures with sharp edges are often numerically simulated in full-physics models (Corbosiero et al. 2006) and are often observed in hurricanes (Kossin and Eastin 2001). The evolution of the central ellipse is also reminscent of the Kida (1981) vortex, and exhibits quasi-elastic behaviour (Dritschel 1990), isolating itself from mixing with the surrounding fluid (cf. Bassom and Gilbert 1999). A final contributing factor to non-axisymmetrization are vortex Rossby waves outside of the central ellipse. A pentapole structure formed with the outer low vorticity structures (with period τ_o; see the top panel of Fig. 5) rotating with a lower angular velocity than the ellipse. This causes alternating tripole and pentapole patterns to exist. The evidence above suggests that non-axisymmetric structures may persist for long times in tropical cyclone cores, potentially leading to prolonged episodes of spontaneous adjustment emission.

Can the oscillation frequency of the central ellipse be explained in a simpler context? It is well known that in a nondivergent barotropic framework an elliptical vortex patch (the Kirchhoff vortex) will rotate with an angular velocity that depends on the magnitude of the vorticity patch ζ, the semi-major axis a, and semi-minor axis b, i.e.,

$$\omega_{\rm KI} = \zeta \frac{ab}{(a+b)^2}, \tag{7}$$

where $\omega_{\rm KI}$ is the angular velocity of the Kirchhoff elliptical vortex. This occurs because when the Poisson equation is solved to obtain the streamfunction, it is less eccentric than the vorticity ellipse leading to vorticity advection (see Fig. 7). Larger vorticity indicates larger winds leading to an increased rotation rate $\omega_{\rm KI}$.

In the numerical simulation, the central ellipse is nearly a constant vorticity patch with magnitude $\zeta = 1.6 \times 10^{-2}$ s^{-1}. In the 24–25 h period, the semi-major axis is $a = 33$ km and the semi-minor axis is $b = 22$ km. Substituting these values into (9), we obtain $\omega_{\rm KI} = 3.84 \times 10^{-3}$ rad s^{-1}. Since the signal is repeated twice for every ellipse rotation, the Kirchhoff ellipse frequency $\nu_{\rm KI} = 2\omega_{\rm KI} = 7.68 \times 10^{-3}$ s^{-1}. Hence, the frequency of a Kirchhoff ellipse is nearly the same as (but slightly greater) the observed frequency, i.e., $\nu_{\rm KI} \approx \nu_{\rm e}$. Therefore, the rotation rate of the simulated central ellipse can largely be explained by a simple Kirchhoff vortex, and because it is slightly larger than the obsered rotation rate, the outer wind field is actually slowing the elliptical vortex down slightly.

In Fig. 7, the azimuthal mean velocity and angular velocity are shown for the spontaneously radiating vortex at $t = 0$, $t = 24$, and $t = 48$ h. The vortex center was defined by the maximum vorticity in the domain. This was obtained by moving a square with a dimension of 23 km over the entire domain, averaging the vorticity in that square, and then determining the grid point in

DOI: 10.1002/qj

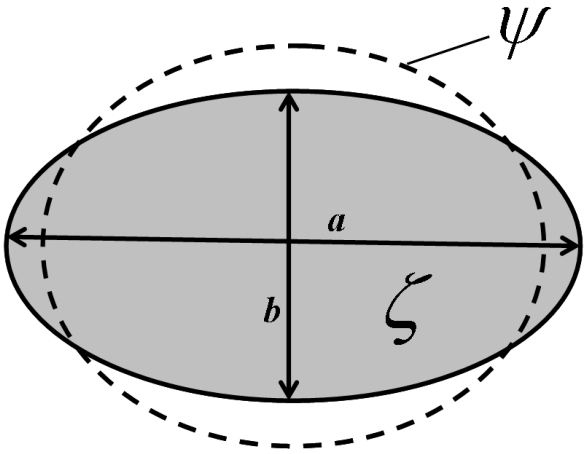

Figure 6. Kirchhoff vorticity ellipse and associated streamfunction. For $\zeta > 0$ the pattern rotates cyclonically at a constant rate, since the streamfunction is less elliptical than the vorticity, a result of the fact that solving the Poisson equation $\nabla^2\psi = \zeta$ for ψ is a smoothing operation.

the square center for which the average vorticity was a maximum. Over the course of the simulation the peak mean tangential winds fell from 100.8 m s^{-1} to 89.0 m s^{-1} in the first 24 hours, and then fell to 86.6 m s^{-1} in the last 24 hours. Thus during the quasi-elastic radiative phase ($t = 24 - 48$ h), the peak winds dropped 3%. Therefore, the outward radiation of spiral IGWs is a sink of tangential (and angular) momentum (consistent with Chow and Chan 2004), albeit very small. Very minor changes occurred in the mean angular velocity. Most notably, the sharp edge became smooth as a result of diffusion. Just outside the vortex core (50 km $< r <$ 150 km), an appropriate choice for $\bar{\omega} = 0.0005$ s^{-1}. For the far field ($r > 150$ km), a more accurate choice is $\bar{\omega} = 0.0001$ s^{-1}. For comparisons to the linear solution just outside the vortex core, we have used the former value (section 4).

In Fig. 8, the domain integrated kinetic energy

$$\mathrm{KE} = \iint_{\mathrm{A}} \rho_0 \mathrm{h} \frac{\mathbf{u}\cdot\mathbf{u}}{2}\,\mathrm{dA} \qquad (8)$$

is shown, using $\rho_0 = 1.13$ kg m^{-3}. The initial KE is 293 pJ. Note that there are two regions of differing slopes. Most kinetic energy is lost between $t = 0$ and $t = 12$ h (15%). From $t = 12$ to $t = 48$ h, the kinetic energy only decreases by by 1.5%. The former phase can be characterized mainly by vorticity mixing, while the latter phase is marked by by spontaneous radiation. This is more evidence that the prolonged episode of spontaneous adjustment emission is not significant for the spin down of the vortex. Also note that the nonconservative momentum sinks of diffusion and the sponge layer are contributing factors to the loss of KE.

The same experiment was executed in a nondivergent model to examine the evolution in the absence of gravity wave emission. The vorticity evolution in both experiments is similar, which is clearly illustrated in Fig. 9. Here the relative vorticity is shown at $t = 30$ h for nondivergent barotropic (left panel) and shallow water (right panel)

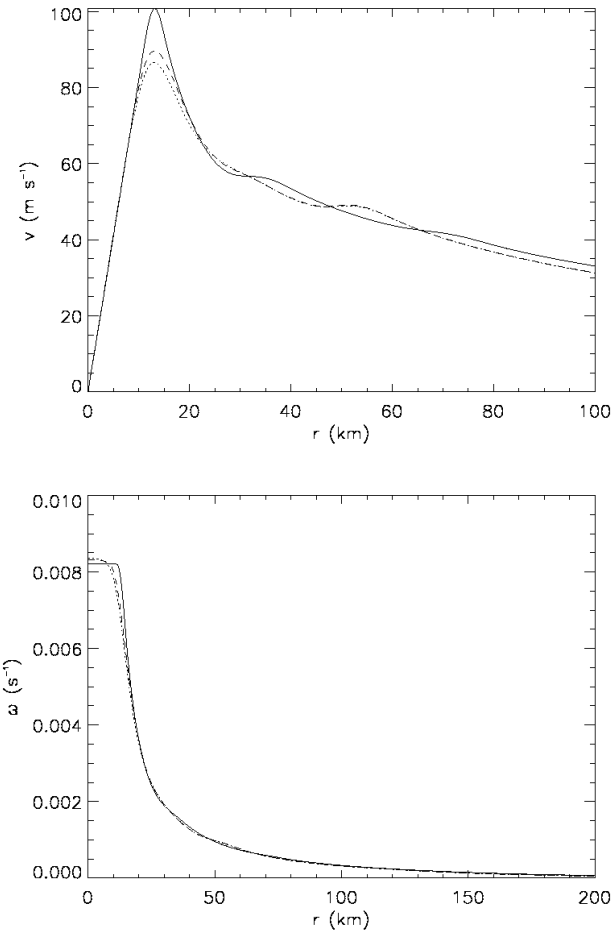

Figure 7. The change in the vortex azimuthal mean velocity (top panel) and angular velocity (bottom panel) over the 48 h numerical simulation. The solid line denotes $t = 0$ h, the dashed line denotes $t = 24$ h, and the dotted line denotes $t = 48$ h. In the top panel, note that the tangential velocity decreases most in the first 24 h.

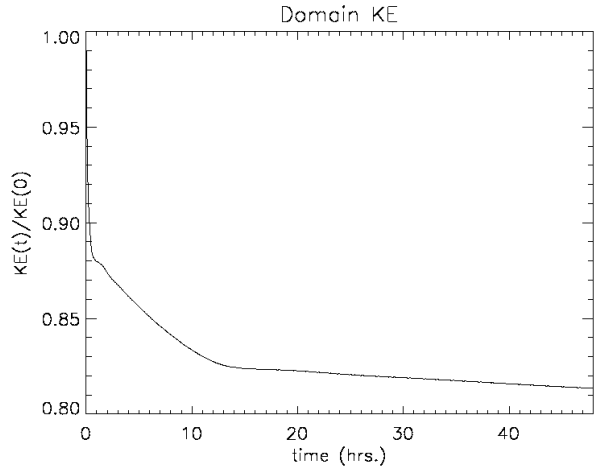

Figure 8. The temporal evolution of the domain integrated kinetic energy (KE).

models. The radial pentapole structure and filaments are similar in each simulation. The primary difference is that the central monopole is *more elliptical* in the shallow

DOI: 10.1002/qj

water model. This is due to the Rossby-IGW instability as discussed by Schecter and Montgomery (2004, 2006) and Hodyss and Nolan (2008).

4 Inertia-gravity waves, multiscale frequency matching and Lighthill emission

Away from the active core region, the flow approximately obeys the linearized versions of (2)–(4), which in polar coordinates are

$$\left(\frac{\partial}{\partial t}+\bar{\omega}\frac{\partial}{\partial\varphi}\right)\delta'-(f+2\bar{\omega})\zeta' + g\left[\frac{\partial}{r\partial r}\left(r\frac{\partial h'}{\partial r}\right)+\frac{\partial^2 h'}{r^2\partial\varphi^2}\right]=0, \tag{9}$$

$$\left(\frac{\partial}{\partial t}+\bar{\omega}\frac{\partial}{\partial\varphi}\right)\zeta'+(f+2\bar{\omega})\delta'=0, \tag{10}$$

$$\left(\frac{\partial}{\partial t}+\bar{\omega}\frac{\partial}{\partial\varphi}\right)h'+\bar{h}\delta'=0, \tag{11}$$

where

$$\delta'=\frac{\partial(ru')}{r\partial r}+\frac{\partial v'}{r\partial\varphi}, \qquad \zeta'=\frac{\partial(rv')}{r\partial r}-\frac{\partial u'}{r\partial\varphi}, \tag{12}$$

with u' denoting the radial component of velocity and v' the azimuthal component of velocity. As is easily checked by direct substitution, the outward propagating IGW solutions of (6) are

$$\begin{pmatrix}\delta'(r,\varphi,t)\\ \zeta'(r,\varphi,t)\\ h'(r,\varphi,t)\end{pmatrix}=h_0\begin{pmatrix}i(\nu-\bar{\omega}m)/\bar{h}\\ (f+2\bar{\omega})/\bar{h}\\ 1\end{pmatrix}H_m^{(1)}(kr)e^{i(m\varphi-\nu t)}, \tag{13}$$

where the Hankel function $H_m^{(1)}(kr)$ is given in terms of the Bessel function $J_m(kr)$ and the Neumann function $Y_m(kr)$ by $H_m^{(1)}(kr)=J_m(kr)+iY_m(kr)$, and where the radial wavenumber k and the frequency ν are related by (6).

The velocity potential and the streamfunction associated with the divergence and vorticity given in the first two lines of (8) are

$$\begin{pmatrix}\chi'(r,\varphi,t)\\ \psi'(r,\varphi,t)\end{pmatrix}=-\frac{h_0}{\bar{h}k^2}\begin{pmatrix}i(\nu-\bar{\omega}m)\\ f+2\bar{\omega}\end{pmatrix}H_m^{(1)}(kr)e^{i(m\varphi-\nu t)}. \tag{14}$$

From (10) we find that the perturbation radial velocity $u'=(\partial\chi'/\partial r)-(\partial\psi'/r\partial\varphi)$ and the perturbation azimuthal velocity $v'=(\partial\chi'/r\partial\varphi)+(\partial\psi'/\partial r)$ can be written as

$$\begin{pmatrix}u'(r,\varphi,t)\\ iv'(r,\varphi,t)\end{pmatrix}=\frac{ih_0}{\bar{h}k^2}\begin{pmatrix}(\nu-\bar{\omega}m+f+2\bar{\omega})(m/r)H_m^{(1)}(kr)\\ -(\nu-\bar{\omega}m)kH_{m-1}^{(1)}(kr)\\ (\nu-\bar{\omega}m+f+2\bar{\omega})(m/r)H_m^{(1)}(kr)\\ -(f+2\bar{\omega})kH_{m-1}^{(1)}(kr)\end{pmatrix}e^{i(m\varphi-\nu t)}, \tag{15}$$

where we have made use of the Hankel function derivative relation $dH_m^{(1)}(kr)/dr=kH_{m-1}^{(1)}(kr)-(m/r)H_m^{(1)}(kr)$. The aymptotic forms for large kr are

$$H_m^{(1)}(kr)\sim\left(\frac{2}{\pi kr}\right)^{1/2}\exp\left[i\left(kr-\frac{m\pi}{2}-\frac{\pi}{4}\right)\right] \tag{16}$$

Note that, in the linear sense, the potential vorticity anomaly associated with these inertia-gravity waves is zero, i.e., $\zeta'-(f/\bar{h})h'=0$.

The linear solutions (12) are shown in Fig. 10 for varying radial wavenumber $k=0.01, 0.025, 0.05$ km^{-1}, while holding the azimuthal wavenumber $m=2$, and f = 0.000037 s^{-1} fixed. The frequency matched radial wavenumber $k=0.028$ km^{-1} most closely matches the middle panels. A comparison of the propagating IGWs in the nonlinear simulation and the linear solution is shown in Fig. 11. The linear solution is obtained with the frequency-matched radial wavenumber $k_{\rm R}=0.028$ km^{-1} and $\bar{\omega}=0.0005$ s^{-1}. In left and right panels, each image is 3 minutes apart. At small radii, the linear solution is not valid, however note the similarities in the solutions for $r>$ 50 km and also that the azimuthal cyclonic propagation of the IGW spiral bands nearly match the spiral bands in the numerical experiment. This is evidence that outside the central ellipse the dynamics can be explained by freely propagating IGWs on a weakly rotating basic state.

To further illustrate the propagating IGWs, in Fig. 12 a plot of the $h'(r,\varphi)$ is shown with the overlayed perturbation wind vectors obtained from (15). The vectors are plotted when $r>100$ km. First note that the wind vectors are perpendicular to the perturbation height, i.e., the winds are completely divergent. Also note that the orientation of the wind vectors with the positive and negative height anomalies favour outward propagation of the waves.

5 Conclusions

A shallow water primitive equation model simulation of a dynamically active, non-axisymmetrizing hurricane-like vortex was analyzed to understand the nature and significance of spontaneous radiation from unsteady vortical motion in the inner-core. The initial condition for the simulation was an offset monopole in an elliptical vorticity ring, which was motivated by observations of elliptically shaped eyewalls in hurricanes. The initially balanced flow evolved quickly into an quasi-balanced state, and outwardly propagating IGWs radiated from the central core, which slowly became more elliptical as the simulation progressed. Two phases of evolution were observed. The first phase (lasting 12 h) was characterized by vorticity mixing and rearrangement, and the second phase (lasting 36 h) was characterized by spontaneous radiation due to multiscale frequency matching between unsteady vortical motion in the core and an intrinsic IGW.

While we find that the IGWs are mostly slaved to the unsteady vortical motion, a nontrivial Rossby-IGW instability causes growth of the vortex Rossby wave on the central monopole. We also find that the most significant

DOI: 10.1002/qj

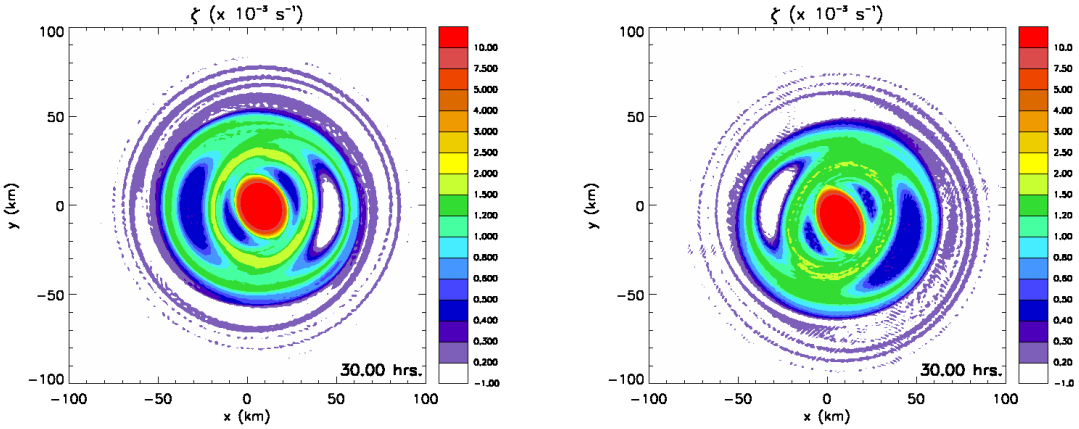

Figure 9. Side-by-side panels of the nondivergent (left) and divergent (right) barotropic model simulations at $t = 30$ h. The initial condition for vorticity and model diffusion are exactly the same in each simulation.

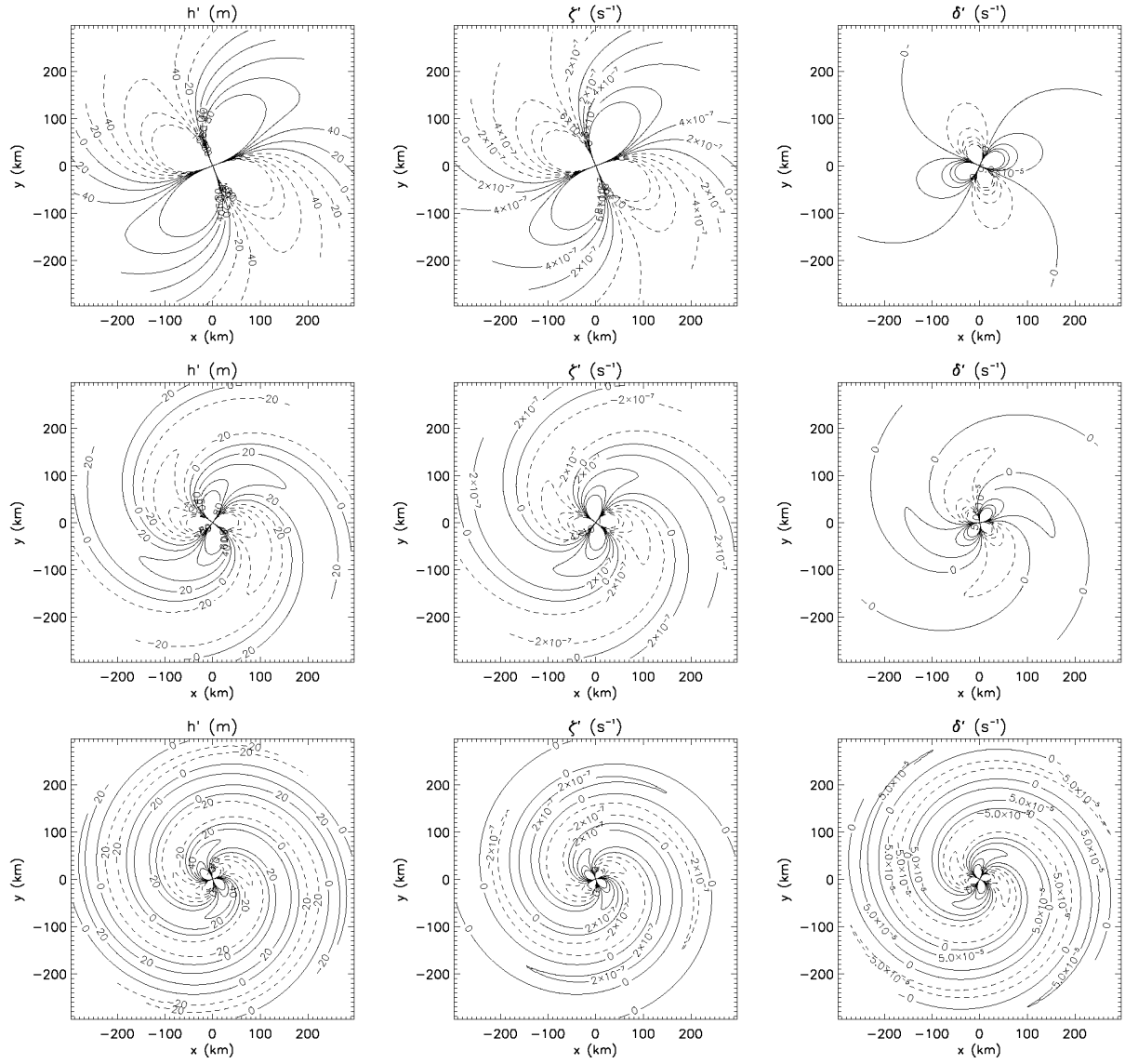

Figure 10. Linear solution to the shallow water equations for varying radial wavenumber: $k = 0.01$ km^{-1} (top row), $k = 0.025$ km^{-1} (middle row), and $k = 0.05$ km^{-1} (bottom row). The azimuthal wavenumber $m = 2$ is held fixed. The contour intervals for h, ζ and δ are 20 m, 2×10^{-7} s^{-1}, and 5×10^{-5} s^{-1}, respectively. The constant h_0 in (9) is set to a value of 100 m.

DOI: 10.1002/qj

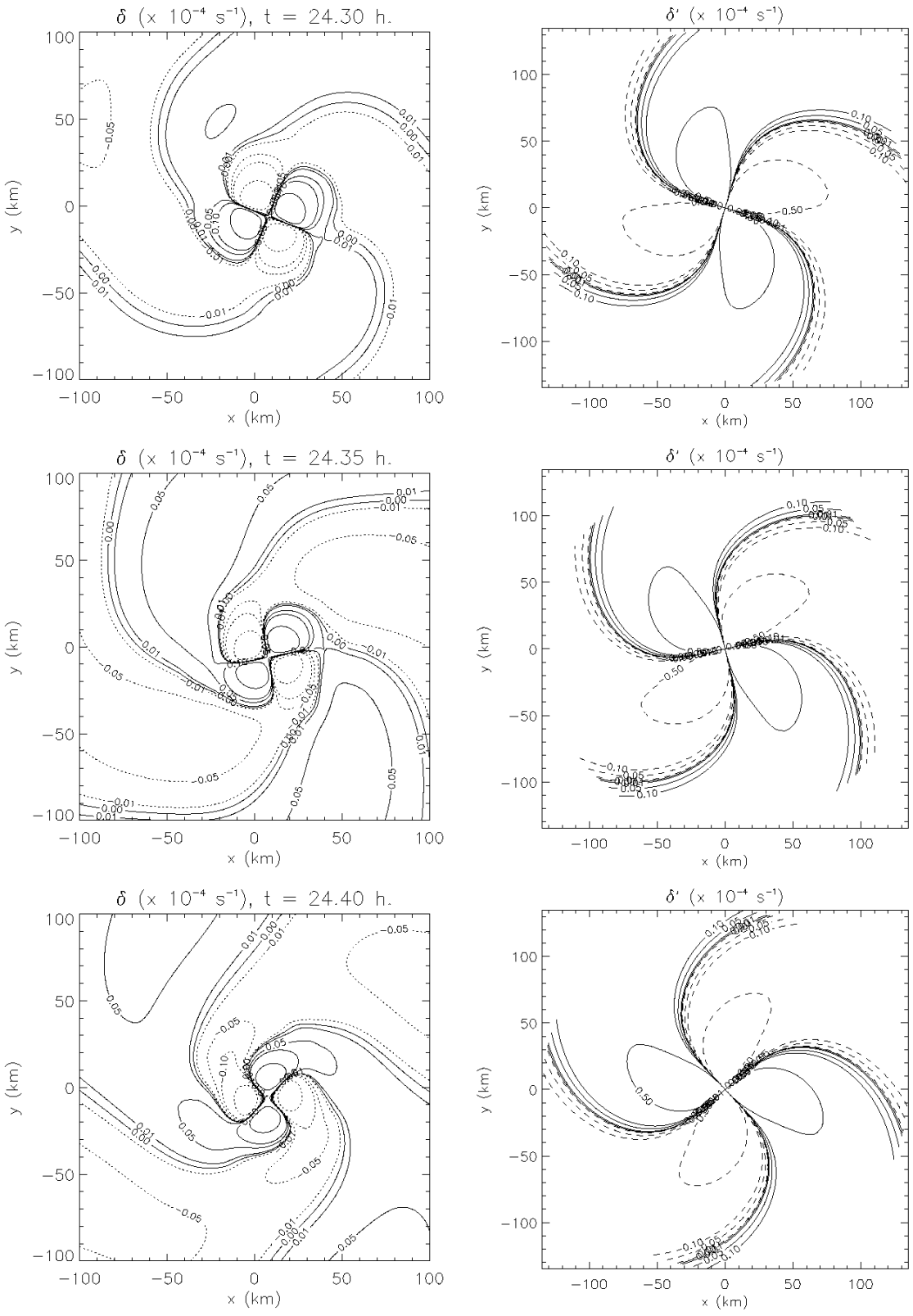

Figure 11. Comparison of the outward propagating IGW in the nonlinear numerical model simulation (left panels) with the linear wave theory (right panels). The linear solution was obtained from the choice $m = 2$ and $k = 0.028$ km^{-1}, the latter of which is suggested by frequency matching with the inner core vortex. Plots are 3 minutes apart.

weakening of the mean vortex occured in the vorticity mixing phase (15% by kinetic energy), while only minor weakening (1.5%) occurred during the radiative phase. It should also be noted that a portion of the total weakening in each phase can be attributed to the nonconservative momentum sinks of diffusion and the sponge layer.

DOI: 10.1002/qj

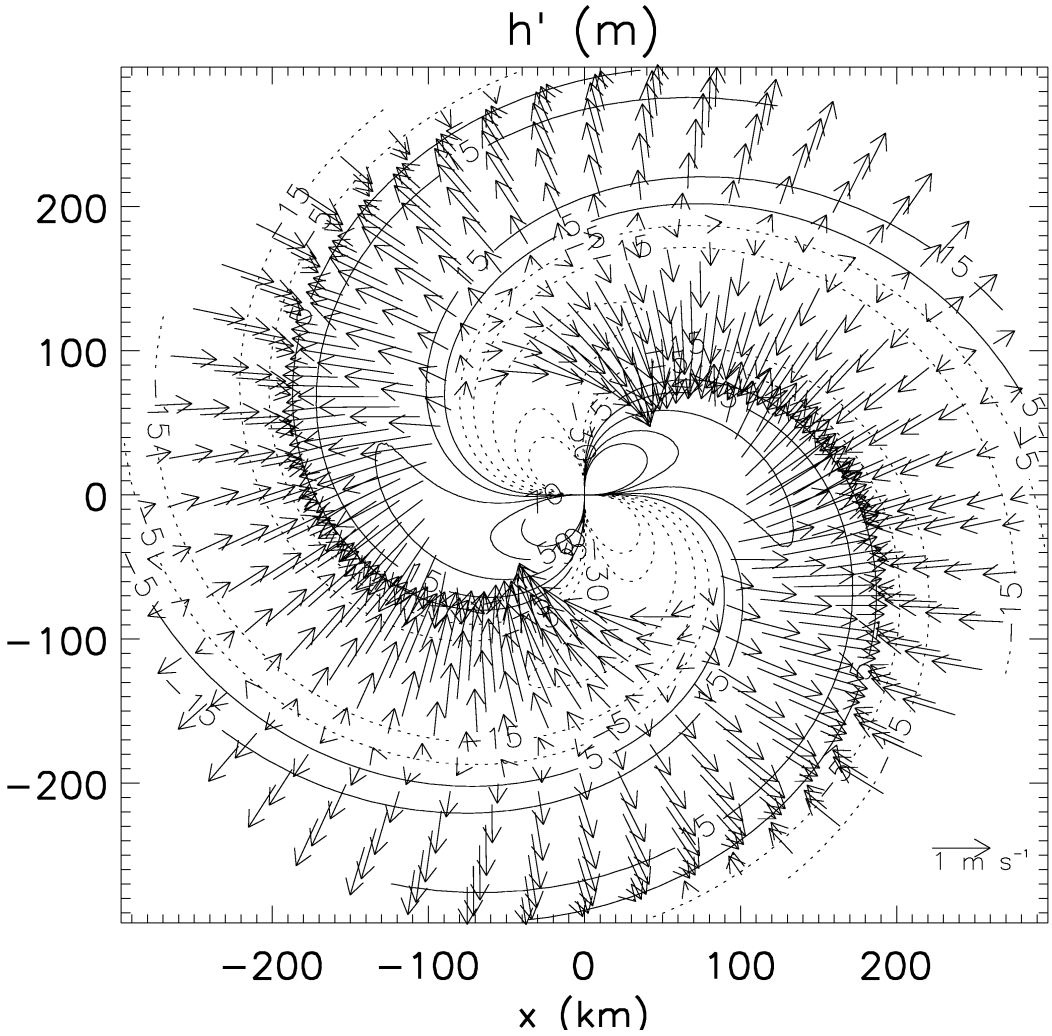

Figure 12. Contours of the perturbation height with overlayed perturbation wind vectors for linear solution.

Broadly, these results indicate that intense hurricanes may enter into spontaneously radiative states, that these states are not likely to be able to be measured due to the small amplitude of the waves, and that the radiation is not significant for intensity change. With regard to internal dynamics, the amplification and decay of tropical cyclones is therefore most strongly affected by vorticity mixing.

Acknowledgements

This research was supported by NSF Grants ATM-0530884 and ATM-0332197, and by NASA/TCSP Grant 04-0007-0031. This research was performed while E.H. was a Ph.D. student at Colorado State University.

References

Afanasyev Y. 2003. Spontaneous emission of gravity waves by interacting vortex dipoles in a stratified fluid: laboratory experiments. *Geophys. Astrophys. Fluid Dyn.* **97**(2): 79–95.

Bassom AP, and Gilbert AD. 1999. The spiral wind-up and dissipation of vorticity and a passive scalar in a strained planar vortex. *J. Fluid Mech.* **398**: 245–270.

Chow KC, Chan KL, and Lau AK. 2002. Generation of moving spiral bands in tropical cyclones. *J. Atmos. Sci.* **59**: 2930–2950.

Chow KC and Chan KL. 2004. Angular momentum transports by moving spiral waves. *J. Atmos. Sci.* **60**: 2004–2009.

Corbosiero KL, Molinari J, Aiyyer AR, and Black ML. 2006. The structure and evolution of Hurricane Elena (1985). Part II: Convective asymmetries and evidence for vortex Rossby waves. *Mon. Wea. Rev.* **134**: 3073–3091.

Dritschel DG. 1990. The stability of elliptical vortices in an external straining flow. *J. Fluid Mech.* **210**: 223–261.

Dritschel DG. 1998. On the persistence of non-axisymmetric vortices in inviscid two-dimensional flows. *J. Fluid Mech.* **371**: 141–155.

Ford R. 1994a. Gravity wave radiation from vortex trains in rotating shallow water. *J. Fluid Mech.* **281**: 81–118.

Ford R. 1994b. The instability of an axisymmetric vortex with monochromatic potential vorticity in rotating shallow water. *J. Fluid. Mech.*, **280**, 303–334.

Ford R, McIntyre ME, and Norton WA. 2000. Balance and the slow quasimanifold: Some explicit results. *J. Atmos. Sci.* **57**: 1236–1254.

Guinn TA and Schubert WH. 1993. Hurricane spiral bands. *J. Atmos. Sci.* **50**: 3380–3403.

Hodyss D and Nolan DS. 2008. The Rossby-inertia-buoyancy instability in baroclinic vortices. *Phys. Fluids. in press.*

Kida, S. 1981. Motion of an elliptic vortex in a uniform shear flow. *J. Phys. Soc. Japan* **50**: 3517–3520.

Kossin JP, and Eastin MD. 2001. Two distinct regimes in the kinematic and thermodynamic structure of the hurricane eye and eyewall. *J.*

Atmos. Sci. **58**: 1079–1090.
Kuo H-C, Williams RT, and Chen J-H. 1999. A possible mechanism for the eye rotation of Typhoon Herb. *J. Atmos. Sci.* **56**: 1659–1673.
Kurihara Y. 1976. On the development of spiral bands in tropical cyclones. *J. Atmos. Sci.* **33**: 940–958.
Leith CE. 1980. Nonlinear normal mode initialization and quasi-geostrophic theory. *J. Atmos. Sci.* **37**: 958–968.
Lighthill MJ. 1952. On sound generated aerodynamically. I. General theory. *Proc. Roy. Soc. London* **A211**: 564–587.
Lorenz EN. 1986. On the existence of a slow manifold. *J. Atmos. Sci.* **43**: 1547–1557.
Lorenz EN, and Krishnamurthy V. 1987. On the nonexistence of a slow manifold. *J. Atmos. Sci.* **44**: 2940–2950.
Lovegrove AF, Read PL, and Richards CJ. 2000. Generation of inertia-gravity waves by a time-dependent baroclinic wave in the laboratory. *Phys. Chem. Earth (B)* **24**(5): 455–460.
Montgomery MT and Kallenbach RA. 1997. A theory for vortex Rossby waves and its application to spiral bands and intensity change in hurricanes. *Quart. J. Roy. Meteor. Soc.* **123**: 435–465.
Montgomery MT and Enagonio J. 1998. Tropical cyclogenesis via convectively forced vortex Rossby waves in a three-dimensional quasi-geostrophic model. *J. Atmos. Sci* **55**: 3176–3207.
Oda M, Nakanishi M, and Naito G. 2006. Interaction of an asymmetric double vortex and trochoidal motion of a cyclone with the concentric eyewall structure. *J. Atmos. Sci.* **63**: 1069–1081.
O'Sullivan D, and Dunkerton TJ. 1995. Generation of inertia-gravity waves in a simulated life cycle of baroclinic instability. *J. Atmos. Sci.* **52**: 3695–3716.
Plougonven R, and Zeitlin V. 2002. Internal gravity wave emission from a pancake vortex: An example of wave-vortex interaction in strongly stratified flows. *Phys. Fluids* **14**: 1259–1268.
Reasor PD, Montgomery MT, Marks FD, and Gamache JF. 2000. Low-wavenumber structure and evolution of the hurricane inner core observed by airborne dual-Doppler radar. *Mon. Wea. Rev.* **128**: 1653–1680.
Saujani S, and Shepherd TG. 2002. Comments on "Balance and the slow quasimanifold: Some explicit results." *J. Atmos. Sci.* **59**: 2874–2877.
Schecter DA, and Montgomery MT. 2004. Damping and pumping of a vortex Rossby wave in a monotonic cyclone: Critical layer stirring versus inertia-buoyancy wave emission. *Phys. Fluids* **16**: 1334–1348.
Schecter DA, and Montgomery MT. 2006. Conditions that inhibit the spontaneous radiation of spiral inertia-gravity waves from an intense mesoscale cyclone. *J. Atmos. Sci.* **63**: 435–456.
Schubert WH, Montgomery MT, Taft RK, Guinn TA, Fulton SR, Kossin JP, and Edwards JP. 1999. Polygonal eyewalls, asymmetric eye contraction, and potential vorticity mixing in hurricanes. *J. Atmos. Sci.* **56**: 1197–1223.
Schubert WH, Hack JJ, Silva Dias PD, and Fulton SR. 1980. Geostrophic adjustment in an axisymmetric vortex. *J. Atmos. Sci.* **37**: 1464–1484.
Snyder C, Muraki DJ, Plougonven R, and Zhang F. 2007. Inertia-gravity waves generated within a dipole vortex. *J. Atmos. Sci.* **64**: 4417–4431.
Uccellini LW and Koch SE. 1987. The synoptic setting and possible energy sources for mesoscale wave disturbances. *Mon. Wea. Rev.* **115**: 721–729.
Vanneste J, and Yavneh I. 2004. Exponentially small inertia-gravity waves and the breakdown of quasigeostrophic balance. *J. Atmos. Sci.* **61**: 211–223.
Viúdez A. 2006. Spiral patterns of inertia-gravity waves in geophysical flows. *J. Fluid Mech.* **562**: 73–82.
Viúdez A, and Dritschel DG. 2006. Spontaneous generation of inertia-gravity wave packets by balanced geophysical flows. *J. Fluid Mech.* **553**: 107–117.
Williams PD, Haine TWN, and Read PL. 2005. On the generation mechanisms of short-scale unbalanced modes in rotating two-layer flows with vertical shear. *J. Fluid Mech.* **528**: 1–22.
Willoughby HE. 1978. A possible mechanism for the formation of hurricane rainbands. *J. Atmos. Sci.* **35**: 838–848.
Willoughby HE. 1990. Gradient balance in tropical cyclones. *J. Atmos. Sci.* **47**: 265–274.
Zhang F. 2004. Generation of mesoscale gravity waves in upper-tropospheric jet-front systems. *J. Atmos. Sci.* **61**: 440–457.

DOI: 10.1002/qj